Check for updates

A polarized broken framework for electrical energy harvesting from mechanical friction

Abdul Khayum Mohammed,†[a] Jelmy Elavathingal Johny,†[b]
José Ignacio Martínez, [ID][c] Mahira Bashri,[a] Nada Elmerhi,[a] Sithara Radhakrishnan,[b]
Ammar Nayfeh, [ID][d] Honey John*[b] and Dinesh Shetty [ID] *[ae]

It is essential to harness energy from every available source to meet the rapidly growing demand. Motion-assisted energy harvesting is an emerging and promising technique to achieve this. Mechanical friction between two surfaces generates charge separation, which results in an electric current that can be captured as usable energy. This principle is utilized in a triboelectric nanogenerator (TENG), which relies on surfaces with appropriate charge characteristics. In this work, we present a novel approach to create a negatively charged surface by using bromine- and oxygen-rich broken frameworks of a 3D covalent organic framework (3D-COF) on a PAN surface (TamDbta-PAN). The TamDbta-PAN was fabricated through *in situ* dripping of TamDbta broken framework spheres from a water–ethylacetate interface onto a PAN surface. Notably, this functionally rich TamDbta-PAN serves as an effective tribonegative layer when paired with a tribopositive nylon-11 layer, achieving a high power density of 2342 mW m^{-2} and demonstrating efficient energy harvesting from mechanical friction.

Covalent organic frameworks (COFs) are two- or three-dimensional (2D/3D) covalent solids composed of organic molecules.[1–5] Notably, many inherent properties of COFs, such as their long porous cavities, originate from their extended polymeric nature.[6–8] The growth of COFs through polymerization and weak molecular interactions often yields extended porous frameworks with the consumption of reactive functional groups (*e.g.*, C=O, NH$_2$, B(OH)$_2$). Interestingly, these reactive functional groups are polar in nature, which is beneficial for many surface-sensitive

New concepts

Covalent organic frameworks (COFs) are porous solids with an extended 2D or 3D molecular framework constructed *via* covalent bonds. Recent developments in defective or "broken" COFs have demonstrated significant advantages over their pristine counterparts. The introduction of defects into COFs creates several beneficial features: (1) defects generate additional channels, which enhance transport efficiency; (2) they introduce numerous functional groups; and (3) they increase the exposure of these functional moieties. Moreover, broken frameworks combine polymeric heterogeneity with molecular-level accessibility, making them particularly promising for energy harvesting applications; however, they are still underexplored. Meanwhile, sustainable harvesting of renewable energy sources is crucial for long-term environmental sustainability, and mechanical friction represents a significant source of nano-electricity. In this work, we successfully demonstrate the fabrication of a robust broken-framework layer *via* the *in situ* deposition of an interfacially synthesized, imine-linked defective framework (TamDbta-PAN) onto a polyacrylonitrile (PAN) substrate. The resulting electronegative and functionality-rich TamDbta-PAN was effectively utilized in a triboelectric nanogenerator (TENG) for harvesting electrical energy from mechanical friction. The fabricated TamDbta-PAN/nylon-11 device achieved a high power density of 2342 mW m^{-2}, highlighting its efficient mechanical-to-electrical energy conversion capabilities.

applications like triboelectric nanogenerators (TENGs). In detail, a TENG is a device that harvests energy from mechanical friction between two surfaces, which depends on the charges associated with the surface instead of the bulk properties of the material.[9,10] In such cases, the exposure of polar functional groups is crucial for an efficient energy harvesting process. While molecules possess many freely available functional groups, they are often highly sensitive to temperature and other environmental conditions. Notably, the functional advantages of small molecules and the stability of polymers can be effectively combined in COFs by introducing defects into their structure. Recent advancements in broken frameworks have demonstrated a way to integrate the benefits of both molecules and polymers.[11,12] Broken frameworks refer to defective COFs generated through post-synthetic treatments or *in situ* reaction control. These frameworks retain

[a] *Department of Chemistry, Khalifa University of Science and Technology, PO Box: 127788, Abu Dhabi, United Arab Emirates. E-mail: dinesh.shetty@ku.ac.ae*

[b] *Inter University Centre for Nanomaterials and Devices, Cochin University of Science and Technology, Cochin-22, India. E-mail: honey@cusat.ac.in*

[c] *Instituto de Ciencia de Materiales de Madrid (ICMM-CSIC), C/Sor Juana Inés de la Cruz 3, 28049 Madrid, Spain*

[d] *Department of Electrical Engineering and Computer Science, Khalifa University of Science and Technology, P.O. Box 127788, Abu Dhabi, United Arab Emirates*

[e] *Center for Catalysis and Separations (CeCaS), Khalifa University of Science & Technology, PO Box: 127788, Abu Dhabi, United Arab Emirates*

† AKM and JEJ made equal contributions to this manuscript.

unreacted functional groups while maintaining structural stability, making them promising candidates for various applications. The broken frameworks feature unreactive functional groups while maintaining the stability of the existing framework of the material. Combining monomeric functional groups and newly created chemical bonds improves the physicochemical properties of the broken frameworks.[11,12]

Meanwhile, TENG operation requires continuous mechanical contact between surfaces, which requires mechanically robust electrodes. However, uniformly fabricating broken frameworks onto 2D electrodes remains highly challenging due to the inherent unprocessability of the material. Additionally, post-chemical treatments for making robust 2D structures may compromise the active functional groups within these broken frameworks.[13] In this context, we have fabricated a broken framework sheet through the *in situ* deposition of an interfacially synthesized imine-linked defective broken framework (TamDbta-PAN) on a polyacrylonitrile (PAN) surface. At the solvent interface, the broken frameworks, rich in electronegative bromine and oxygen atoms (from the carbonyl group), were deposited onto the PAN by gravity-driven dripping of the TamDbta frameworks. Notably, the electronegative, functional-rich TamDbta-PAN acts as an effective tribonegative layer against a tribopositive nylon-11 layer. As a result, the TamDbta-PAN/nylon-11 triboelectric device exhibited a high power density of 2342 mW m^{-2}, indicating efficient power transfer and demonstrating effective mechanical energy harvesting in the form of electrical energy. Notably, the TamDbta-PAN/nylon-11 device powered 100 blue LEDs and a wristwatch through simple hand tapping, demonstrating the practical utility of broken frameworks for converting body movements into electrical energy.

The TamDbta-PAN was fabricated by *in situ* deposition of TamDbta on the surface of a PAN membrane during the interfacial synthesis (Fig. 1a and SI2). Herein, the interfacial synthesis of TamDbta was carried out in a water–ethylacetate system by taking a mixture of tetrakisaminophenylmethane (Tam; 0.039 mmol) and *p*-toluenesulphonic acid (*p*-TSA; 0.157 mmol) in water and 2,5-dibromoterephthaldehyde (Dbta; 0.078 mmol) in ethylacetate. The PAN membrane was kept at the bottom of the reaction vessel. During the progress of the reaction, TamDbta was formed at the water–ethylacetate interface, and some spherical particles of TamDbta dripped from this interface onto the PAN surface. This reaction was allowed for 5 days to ensure a uniform *in situ* coating of TamDbta on the PAN membrane. Afterward, the TamDbta-PAN was thoroughly washed with water and acetone to eliminate monomeric impurities. The resulting dried PAN membrane exhibited a bright yellow color, similar to that of pristine TamDbta (Fig. 1b).
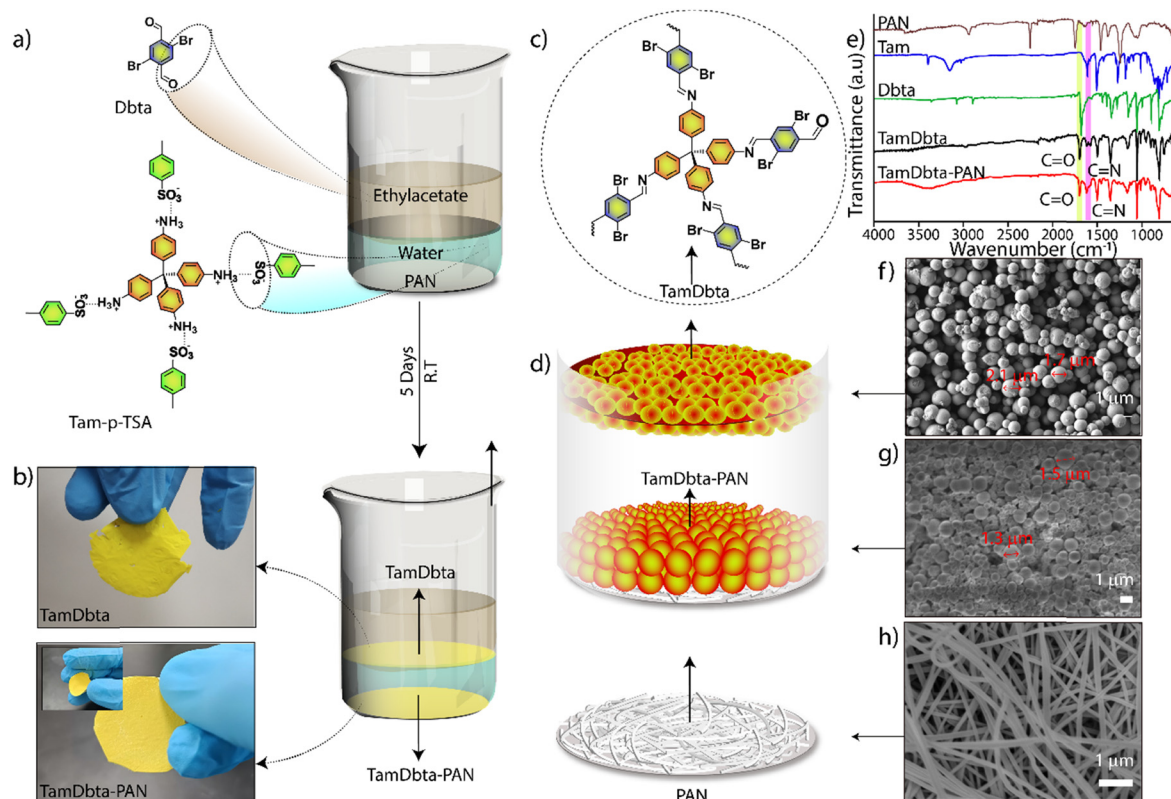

Fig. 1 (a) The graphical representations of the interfacial synthesis of TamDbta-PAN. (b) The digital photographs of TamDbta and TamDbta-PAN (inset: the mechanical flexibility of TamDbta-PAN). (c) The chemdraw of a fraction of TamDbta with the presence of C=O. (d) The graphical representation of the PAN surface, TamDbta-PAN, and TamDbta at the water–ethylacetate interface. (e) The FT-IR spectra of TamDbta-PAN, TamDbta, and the corresponding monomers. The SEM images of (f) TamDbta, (g) TamDbta-PAN, and (h) the PAN surface.

The Fourier transform infrared (FT-IR) spectra of TamDbta-PAN showed a chemical bonding profile similar to that of pristine TamDbta, with peaks corresponding to C=N and C=O bonds at 1617 cm^{-1} and 1695 cm^{-1}, respectively. These peaks confirm the formation of imine bonds and the presence of unreacted C=O groups in the TamDbta (Fig. 1c–e). The absence of any NH$_2$ peaks confirms the complete utilization of amine-functional groups for framework formation. It indicates that the frameworks are discontinued at the carbonyl-end in the Dbta linker. This carbonyl-end termination of the broken framework could be due to the limited molecular transport of Tam + p-TSA from the aqueous phase to the organic phase during the progress of the reaction.[14] The limited number of Tam and abundant number of Dbta at the organic phase results in the full consumption of –NH$_2$ groups and leaving C=O groups at the defective sites.

Furthermore, the ^{13}C CP MAS solid-state NMR analysis of the interfacially formed TamDbta showed the presence of peaks corresponding to C=O (at 186.6 ppm) and C=N (at 155 ppm) (Fig. S1). Again, the interfacially formed TamDbta displayed a moderate crystallinity in powder X-ray diffraction (PXRD), characterized by two broad peaks at two theta angles of $\sim$6.9° and 12.5° (Fig. S2). However, these crystalline peaks of TamDbta were absent in the PXRD of TamDbta-PAN, which could be due to the low thickness of the TamDbta on PAN and the relatively lower crystallinity of the TamDbta itself. The moderate crystallinity of TamDbta can be attributed to two primary factors: (1) the defective nature of TamDbta, which hinders the formation of large, extended frameworks, and (2) the presence of large bromine atoms, which induce steric effects that restrict the formation of a crystalline network.

The scanning electron microscopic (SEM) images of TamDbta-PAN showed the deposition of spherical particles ($\sim$1–2 μm) of broken frameworks on the surface of the interwoven structured PAN surface (Fig. 1d and f–h). Notably, the SEM images of interfacial TamDbta revealed its bottom layer morphology of spherical nature ($\sim$1–2 μm). Interestingly, these spheres are dripped from the TamDbta formed at the water–ethylacetate interface onto the PAN surface placed on the bottom of the reaction vessel. The distribution of spherical particles covered the entire surface of the PAN with uniform thickness ($\sim$4–6 μm) (Fig. S3).

The SEM images of TamDbta-PAN, TamDbta, and PAN clearly show that spherical particles of TamDbta transfer from the interface to the PAN surface during the reaction period. Thus, it is important to understand the chemical and morphological changes occurring throughout the deposition process. In this regard, the TamDbta-PAN and pristine TamDbta were analyzed every day for five days of interfacial reaction using FT-IR and SEM (Fig. 2a–d). Notably, the FT-IR results indicate the formation of TamDbta (C=N at 1617 cm^{-1}) at the water–ethylacetate interface on the 1st day of the reaction (Fig. 2d). Importantly, the initial formation of small spheres (diameter of $\sim$100–800 nm) is observed in the SEM images (Fig. 2a and Fig. S4). The scattered distribution of these spheres on the PAN membrane indicates the lesser number of spheres dripping

from the interface initially. From day 2 to day 5, the sizes of these spheres increased up to a diameter of $\sim$1–2 μm, and subsequently, the dripping intensity also increased (Fig. 2b and c). The TamDbta is uniformly coated on the surface of PAN from day 4 to day 5, indicated by the invisible interwoven structures of PAN. The FT-IR profile of pristine TamDbta on days 1 to 5 showed a large intensity of C=O (at 1695 cm^{-1}) compared to the C=N (at 1617 cm^{-1}). This implies a high degree of defects within the framework formed at the interface. The TamDbta-PAN exhibits similar intensities for the C=O peak (at 1695 cm^{-1}) and the C=N peak (at 1617 cm^{-1}), suggesting a relatively higher degree of imine-bonds in TamDbta-PAN compared to TamDbta at the interface. This could be attributed to the following reasons: The synthesis of TamDbta occurs at the interface of the solvent system. Here, frameworks are formed with varying degrees of extension. Notably, spheres of TamDbta with longer framework extensions are transferred from the interface and deposited on the PAN surface, which results in a higher degree of imine-bonds in TamDbta-PAN.

Notably, the TamDbta deposition over the PAN altered the hydrophobicity of the surface (Fig. S5). The bare PAN showed a water contact angle of 91°, and the water droplet wet the surface immediately (within <5 s). Meanwhile, the TamDbta deposition enhanced the hydrophobicity of the surface to a water contact angle of 128°, and the water droplet could remain as a drop until it was removed by a syringe needle (Fig. S6). The hydrophobicity of triboelectric layers is important for minimizing the adverse effect of moisture adsorption and retarding performance. To further elucidate the surface properties of TamDbta-PAN, we measured the zeta potential to quantify the magnitude of its surface charge (Fig. S7). The results revealed that the increase in the deposition of TamDbta on PAN from day 2 to day 5 resulted in a pronounced decrease in zeta potential value, from −21.13 to −33.43 mV, respectively. This strong negative surface charge is advantageous for triboelectric nanogenerators, as it enhances electron transfer efficiency when paired with tribopositive materials. The negative charge of TamDbta originates from the electronegative heteroatoms such as N, O, and Br within the framework. In particular, Br is a strongly electron-withdrawing and highly polarizable atom, which increases the surface electronegativity of the broken framework and promotes efficient charge retention.[10d] Overall, the synergistic contributions from Br, N (C=N), and O-rich sites (C=O) generate a strongly electronegative surface for the TamDbta. Moreover, the dielectric permittivity of TamDbta, which is peeled from the TamDbta-PAN, exhibited an enhanced dielectric permittivity, could be due to the polar functional groups present in the TamDbta framework (Fig. S8).

Furthermore, we have explored the mechanical energy harvesting properties of TamDbta-PAN in the TENG considering its higher exposure of electronegative surfaces. The TENG generally consists of two layers: the upper tribopositive and lower tribonegative. The regular contact and separation of these layers result in a charge separation and subsequent charge accumulation on the electrodes, which further creates a
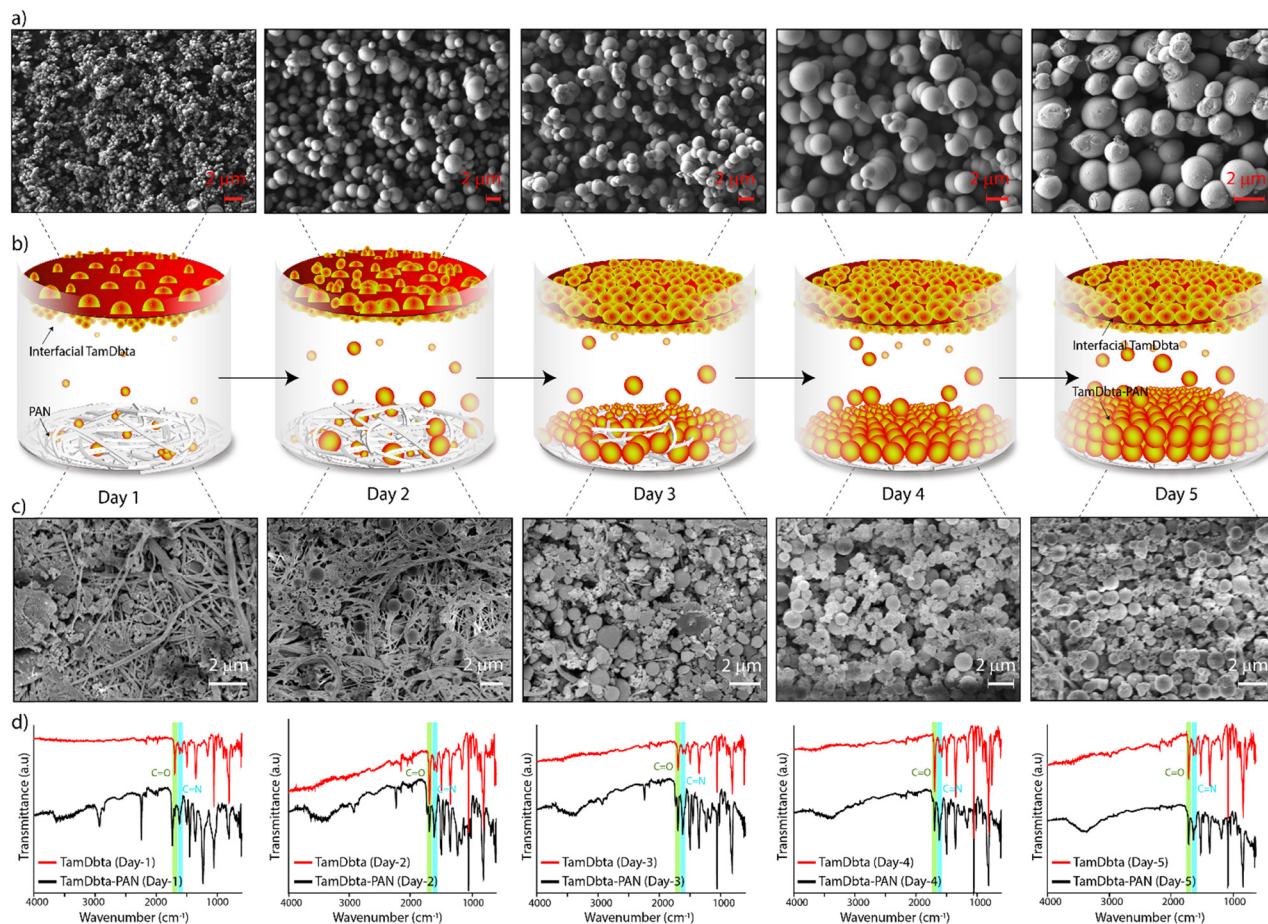
Fig. 2 The mechanism study of the growth of TamDbta–PAN from day-1 to 5. (a) The SEM images of TamDbta at the water−ethylacetate interface from day 1 to 5. (b) The graphical representation of the interfacial reaction. It shows both the growth of TamDbta and TamDbta–PAN. (c) The SEM images of TamDbta–PAN from day 1 to 5. They show the presence of interwoven structures of PAN in the initial days that are gradually covered with spherical particles of TamDbta. (d) The FT-IR spectra of TamDbta and TamDbta–PAN from day 1 to 5.

potential difference across the electrodes (Fig. 3a and Fig. S9).[9,10,15] The TamDbta-PAN was investigated as the tribonegative material (with a size of 1 cm^2) with different types of tribopositive material to understand the functional control effect of the charge separation. Herein, TamDbta-PAN was paired with proactive copper (metallic), fluorinated ethylene propylene (FEP: fluorine-rich organic polymer), and doctor-blade fabricated nylon 11 film (amide-linked organic polymer). According to the triboelectric series, nylon 11 and copper are generally considered tribopositive, meaning that they tend to lose electrons and become positively charged. On the other hand, FEP (fluorinated ethylene propylene) is tribonegative because it tends to gain electrons and become negatively charged, largely due to the presence of highly electronegative fluorine atoms in its structure.[16]

The triboelectric responses of TamDbta-PAN against copper, FEP, and nylon 11 were measured, including open circuit voltage (V_{oc}), short-circuit current (I_{sc}), and charge (Q) (Fig. 3b–d). Notably, the triboelectric responses, including V_{oc}, I_{sc}, and Q, were the highest when the TamDbta-PAN was paired with nylon 11, with values of 43.56 V, 8.86 μA, and 13.76 nC,

respectively. Herein, nylon 11, with a polyamide-connected alkyl backbone, showed a tribopositive (tendency to lose electrons) nature when it is in frictional contact with bromine, an imine nitrogen, and carbonyl-containing TamDbta-PAN. In contrast, the lowest TENG responses were recorded when the TamDbta-PAN was paired with FEP, with V_{oc}, I_{sc}, and Q measured as 5.16 V, 0.81 μA, and 0.48 nC, respectively. Since FEP is a tribonegative material because of the presence of several fluorine atoms, pairing it with TamDbta-PAN, which has also become tribonegative, resulted in weaker TENG responses. The contrast performance of TamDbta-PAN against two linear polymers with different functionalities (amide and fluorine) signifies the critical role of functional groups in surface-sensitive triboelectric applications. Interestingly, when the TamDbta-PAN is paired with copper, it results in a relatively lower triboelectric response compared to nylon 11. Nylon's surface gives up electrons readily, making it a tribopositive surface. In particular, nylon can accumulate a higher positive charge when rubbed against other materials due to its molecular structure, which supports significant charge transfer during contact and separation. Copper, being a metal with
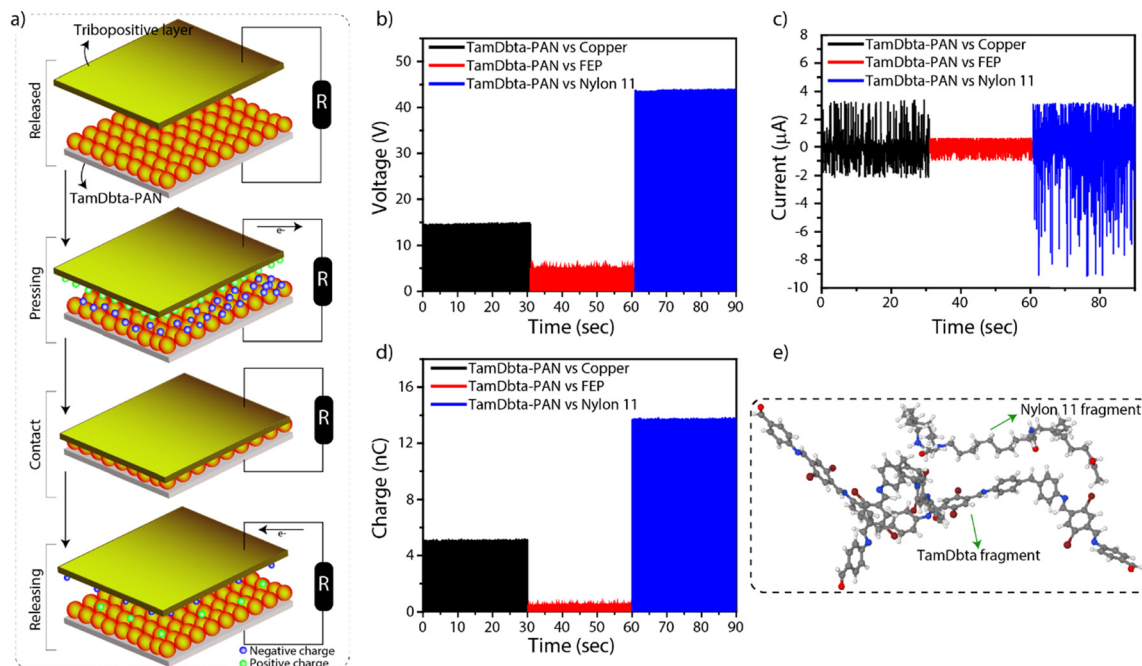
Fig. 3 (a) The graphical representation of the working mechanism of the TamDbta-PAN-based TENG in contact and separation mode. (b) The plot of voltage (V) vs time (s): V_{oc}, (c) the plot of current (μA) vs. time (s): I_{sc}, and (d) the plot of charge (nC) vs. time (s): Q when TamDbta-PAN was paired with copper, FEP and nylon 11. (e) The DFT model of the interaction between the fragments of TamDbta and nylon 11. It shows the geometrical flexibility of nylon 11 when it interacts with TamDbta.

high electrical conductivity, doesn't accumulate charge in the same way. Instead, it tends to allow charge to flow freely, which can reduce its apparent tribopositive nature.[17a–d]

As a proof of concept, we have carried out a series of density functional theory (DFT) calculations using the localized basis set Gaussian16 atomistic simulation package[18] at the B3LYP/6-311** level of theory[19] to explore the nature of the interactions of TamDbta with nylon 11, and fluorinated ethylene propylene (FEP) representative fragments, and with a copper cluster (Cu$_7$) (Fig. S10). These calculations revealed notable interactions between TamDbta and the trial adsorbates, exhibiting a particularly strong electrostatic attraction with the nylon-11 fragment. The calculated physisorption energy for the nylon-11/TamDbta complex was found to be 0.7 eV, significantly higher than the 0.26 eV observed for the TamDbta–FEP system. This difference arises from the remarkable conformational flexibility of nylon-11, which allows closer molecular contact and more favorable electrostatic alignment (Fig. 3e), in contrast to the electrostatic repulsion observed in the FEP system, where both fragments bear negative charge densities. In the case of Cu$_7$, the interaction with the TamDbta fragment indicated a strong chemisorption, although such bonding is unlikely in practical triboelectric layers due to the purely metallic nature of the copper layer (Fig. S11a). Importantly, the nylon-11@TamDbta system exhibited a substantial reduction in electronic band gap from 5.58 eV (for the isolated nylon 11 unit) to 2.97 eV, approaching that of the TamDbta fragment alone (3.18 eV) (Fig. S11b). This ≈0.2 eV gap closure, despite the absence of covalent bonding and underlying chemistry, suggests

significant electronic polarization and charge delocalization at the interface, driven solely by electrostatic interactions. This is further supported by a clear lifting of degeneracy in the HOMO and LUMO states in TamDbta upon interaction with the nylon 11 fragment, pointing to strong interfacial perturbation and orbital distortion effects, even without explicit chemical bonding.

These interfacial electronic effects may offer a compelling explanation for the high power density (2342 mW m^{-2}) observed in the TamDbta–nylon 11 triboelectric device. The pronounced electrostatic interaction and electronic polarization at the interface likely enhance the charge redistribution efficiency and increase surface potential differences during contact-separation cycles, thereby improving the overall energy conversion performance. The synergistic combination in this particular case of strong physisorption, reduced band gap, and interfacial orbital distortion supports the interpretation that nylon 11 is not only a mechanically compatible substrate, but also an electronically active partner in triboelectric energy harvesting.

The spheres of TamDbta completely covered the PAN surface. To understand the triboelectric response of pristine PAN, it was paired with copper, FEP, and nylon 11. Notably, the triboelectric responses of V_{oc} (16.42 V), I_{sc} (0.97 μA), and Q (5.44 nC) were excellent with FEP and relatively lower performance was observed with nylon 11 (Fig. S12–S14). The lowest TENG responses were observed when PAN was paired with copper (0.67 V, 0.12 μA, 0.24 nC). This clearly indicates the tribopositive nature of the pristine PAN. Moreover, this trend in

TENG outcome is consistent with the principle that greater differences in the triboelectric series between two materials can lead to higher TENG responses. Since PAN and copper are close to each other in the triboelectric series, they produced relatively weak TENG responses compared to PAN paired with FEP or nylon 11.[16] In short, the tribopositive nature of PAN was switched into tribonegative upon *in situ* coating of TamDbta.

The tribopair consisting of TamDbta-PAN and nylon 11, which provided the best TENG output, was selected for further analysis. The effect of force on the frictional contact of the trioactive materials was initially examined at a fixed frequency of 10 Hz. The TENG measurements of TamDbta-PAN (days 3 to 6) showed performance rising from day 3 (33.6 V, 5 μA, 10.8 nC) to a maximum at day 5 (43.56 V, 8.86 μA, 13.76 nC), followed by saturation at day 6 (43.96 V, 7.1 μA, 11.76 nC) (Fig. S15). The optimum performance at day 5 could be due to uniform coating, while incomplete (day 3) or excessive (day 6) deposition limited the output. Hence, TamDbta-PAN at day 5 was selected for further analysis.

The electrical output displayed a linear relationship with force in some cases,[17] while in others, it reached a saturation point at higher force levels (Fig. S17–S19).[20,21] A moderate increase in TENG output was observed when the force was varied from 1 N (39.07 V, 3.91 μA, 12.99 nC) to 5 N (40.07 V, 7.52 μA, 13.67 nC). However, the electrical output did not change significantly when the contact force was increased from 5 N to 10 N (43.56 V, 8.86 μA, 13.76 nC).

The highest performance was observed at 10 N force, so further analyses were conducted at this force. The relationship between triboelectric responses and the applied frequency was investigated while maintaining a constant force of 10 N (Fig. 4a–c). The values of V_{oc}, I_{sc}, and charge experienced an enhancement when the frequency was increased from 2 Hz (14.25 V, 2.84 μA, and 8.34 nC) to 10 Hz (43.8 V, 8.86 μA, and 13.76 nC). Increased TENG responses with higher contact frequencies and separation between the tribactive materials are primarily due to generating more triboelectric charges, as frequent interactions lead to greater charge accumulation. Additionally, the shorter intervals between these events reduce the possibility of charge dissipation, allowing more charges to be collected and utilized efficiently. This frequent cycling also enhances charge transfer efficiency between materials, resulting in a stronger triboelectric effect and higher electrical output. Furthermore, the power density was evaluated under a constant force of 10 N at 10 Hz. The voltage and current profiles are analyzed at varying load resistance at 10 N and 10 Hz (Fig. S20). The peak current and voltage across different load resistors were calculated and plotted for power measurements (Fig. 4d). As the resistance increased from 1 MΩ to 1 GΩ, the current decreased from 8.86 μA to 0.28 μA, while the voltage increased from 5.52 V to 43.8 V. Using the power relation $P_{max} = V_{max} \times I_{max}$, a power density of 2342 mW m^{-2} was achieved around 14 MΩ (Fig. 4e). This excellent power density suggests the potential of the broken frameworks for motion-assisted energy harvesting applications. Importantly, the SEM image of TamDbta-PAN showed the distribution of spherical particles even after 25 000 mechanical hits with nylon 11, indicating the stability of the layer (Fig. S19). The consistent open-circuit voltage observed over 50 000 cycles (Fig. S21) demonstrates the durability of TamDbta-PAN under mechanical impact.
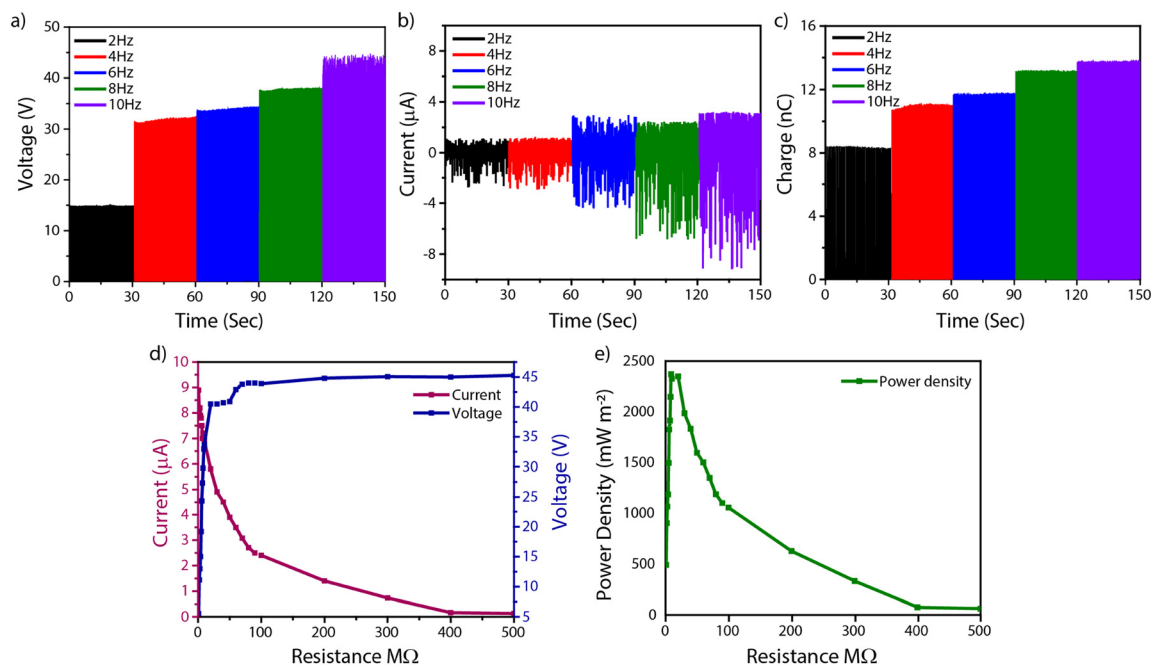

Fig. 4 Effect of frequency on TENG responses: (a) V_{oc}, (b) I_{sc}, and (c) Q when TamDbta-PAN was paired with nylon 11. All triboelectric measurements were conducted at a force of 10 N. (d) Voltage and current profiles were observed using different load resistances. (e) The power density profile for various load resistors.
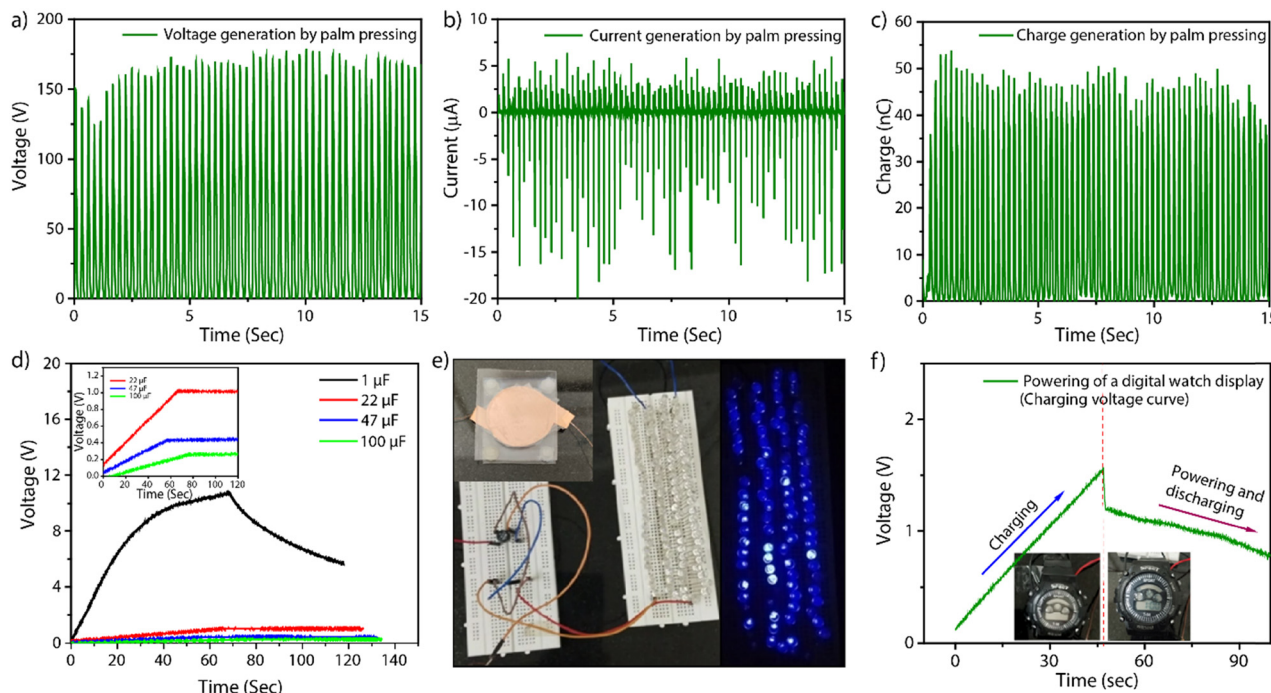
Fig. 5 TENG responses: (a) open-circuit voltage (V_{oc}), (b) short-circuit current (I_{sc}), and (c) charge (Q) generated from the TENG device during palm pressing. (d) Capacitor charging profiles, (e) image showing the powering of LEDs, and (f) charging and powering of a digital watch display.

Furthermore, to demonstrate the practical utility of TamDbta-PAN for harvesting energy from daily-life activities, we have made a TamDbta-PAN/nylon 11 device. To construct the TENG-based device (inset in Fig. 5e), a circular TamDbta-PAN sample with a diameter of 3.5 cm was paired with a nylon 11 film prepared using the doctor blade technique. Both triboelectric materials were attached to copper electrodes of matching dimensions and mounted onto a polymer substrate. Squeezable spacers were incorporated to maintain a uniform gap between the top and bottom triboelectric layers, enabling effective contact and separation during palm pressing. The resulting device was used to generate power to operate portable electronics and charge capacitors through manual palm pressing. The output voltage, current, and charge produced by hand-pressing the TENG module's top surface were recorded while palm pressing (Fig. 5a–c). During palm pressing, the device achieved an average voltage of 170 V, a current of 17 μA, and a charge of 48 nC. The charging performance of the TENG device was assessed under continuous palm pressing (Fig. 5d). It shows capacitances ranging from 1 μF to 100 μF. The device exhibited notable charging rates, reaching 0.27 V s^{-1} for a 1 μF capacitor, 0.02 V s^{-1} for 22 μF, 0.008 V s^{-1} for 47 μF, and 0.003 V s^{-1} for 100 μF, all calculated over a 30-second duration of palm pressing. The same TENG device was utilized to power blue LEDs (~100 numbers) connected in series, as depicted in Fig. 5e and demonstrated in Video S1. A 22 μF capacitor was initially charged to power a watch display through hand pressing on the device. The watch was connected across it once the capacitor was charged to 1.5 V. The watch began to display and turned off as hand pressing ceased and the capacitor

discharged (Fig. 5e and Fig. S22). Video S1 demonstrates the process of charging capacitors through hand pressing, enabling the illumination of LEDs and powering a watch display *via* palm pressing. The FT-IR profile of palm-pressed TamDbta-PAN showed retained peaks of C=O (1697 cm^{-1}) and C=N (1619 cm^{-1}) indicating the structural integrity of TamDbta with PAN during the mechanical contact (Fig. S23). These results clearly indicate the potential of broken frameworks in real-life applications to convert body movement to electrical energy form.

Conclusions

In conclusion, using an *in situ* deposition method, we present a simple strategy for fabricating bromine and oxygen-rich functional broken framework membranes. The broken frameworks of TamDbta are deposited on a PAN surface from an *in situ* growing 3D-COF at a water–ethylacetate interface. Notably, the electronegative functional-rich TamDbta-PAN acts as an effective tribonegative layer when paired with a tribopositive nylon-11 layer, achieving a high power density of 2342 mW m^{-2} and demonstrating efficient energy harvesting from mechanical friction. Furthermore, the device-level applications of the broken frameworks showed their practical utility to convert body movements to electrical energy. Looking forward, the concept of functional broken frameworks opens new opportunities in TENGs and beyond. The flexible and stable nature of the broken framework 2D macrostructures could be further explored for wearable and large-area flexible energy harvesters.

Author contributions

Conflicts of interest

There are no conflicts to declare.

Data availability

Data are available upon request from the authors.

Supporting information: Experimental section. See DOI: https://doi.org/10.1039/d5mh01318f.

Acknowledgements

Notes and references

1 A. P. Cote, A. I. Benin, N. W. Ockwig, M. O'Keeffe, A. J. Matzger and O. M. Yaghi, *Science*, 2005, **310**, 1166.

2 S. Kandambeth, A. Mallick, B. Lukose, M. V. Mane, T. Heine and R. Banerjee, *J. Am. Chem. Soc.*, 2012, **134**, 19524–19527.

3 C. R. DeBlase, K. E. Silberstein, T. T. Truong, H. D. Abruna and W. R. Dichtel, *J. Am. Chem. Soc.*, 2013, **135**, 16821–16824.

4 S. Y. Ding and W. Wang, *Chem. Soc. Rev.*, 2013, **42**, 548–568.

5 K. C. Ranjeesh, S. Kaur, A. K. Mohammed, S. Gaber, D. Gupta, K. Badawy, M. Aslam, N. Singh, T. Skorjanc, M. Finšgar, J. Raya, T. C. Nagaiah and D. Shetty, *Adv. Energy Mater.*, 2024, **14**, 2303068.

6 K. Geng, T. He, R. Liu, S. Dalapati, K. Tian Tan, Z. Li, S. Tao, Y. Gong, Q. Jiang and D. Jiang, *Chem. Rev.*, 2020, **120**, 8814–8933.

7 A. K. Mohammed and D. Shetty, *Environ. Sci.: Water Res. Technol.*, 2021, **7**, 1895–1927.

8 Z. Wang, C. Wang, Y. Chen and L. Wei, *Adv. Mater. Technol.*, 2023, **8**, 2201828.

9 F.-R. Fan, Z.-Q. Tian and Z. L. Wang, *Nano Energy*, 2012, **1**, 328–334.

10 (*a*) C. Wu, A. C. Wang, W. Ding, H. Guo and Z. L. Wang, *Adv. Energy Mater.*, 2019, **9**, 1802906; (*b*) H. F. Mark and S. H. Atlas, *Polym. Eng. Sci.*, 1965, **5**, 204–207; (*c*) J. Zhao and Y. Shi, *Adv. Funct. Mater.*, 2023, **33**, 2213407; (*d*) L. Zhai, S. Cui, B. Tong, W. Chen, Z. Wu, C. Soutis, D. Jiang, G. Zhu and L. Mi, *Chem. – Eur. J.*, 2020, **26**, 5784–5788; (*e*) A. Priyadarshini, S. Divya, J. Swain, N. Das, S. Swain, S. Hajra, S. Panda, R. Samantaray, M. Belal, K. R. Kaja, N. Kumar, H. J. Kim, T. H. Oh, V. Vivekananthan and R. Sahu, *Nanoscale*, 2025, **17**, 1790–1811; (*f*) A. Babu, N. Madathil, R. K. Rajaboina, H. Borkar, K. C. Devarayapalli, Y. K. Mishra, S. Hajra, H. J. Kim, U. K. Khanapuram and D. S. Lee, *Mater. Adv.*, 2025, **6**, 4725–4737; (*g*) G. Khandelwal, D. A. John, V. Vivekananthan, N. Gadegaard, D. M. Mulvihill and S.-J. Kim, *Nanoscale*, 2025, **17**, 3211–3220; (*h*) S. I. Tushar, A. Sayam, M. M. Uddin, T. M. Dip, H. R. Anik, M. R. A. Arin and S. Sharma, *J. Mater. Chem. A*, 2023, **11**, 19244–19280.

11 A. K. Mohammed, A. A. A. Khoori, M. A. Addicoat, S. Varghese, I. Othman, M. A. Jaoude, K. Polychronopoulou, M. Baias, M. A. Haija and D. Shetty, *Angew. Chem., Int. Ed.*, 2022, e202200905.

12 S. Zhao, C. Jiang, J. Fan, S. Hong, P. Mei, R. Yao, Y. Liu, S. Zhang, H. Li, H. Zhang, C. Sun, Z. Guo, P. Shao, Y. Zhu, J. Zhang, L. Guo, Y. Ma, J. Zhang, X. Feng, F. Wang, H. Wu and B. Wang, *Nat. Mater.*, 2021, **20**, 1551–1558.

13 J. L. Segura, S. Royuela and M. M. Ramos, *Chem. Soc. Rev.*, 2019, **48**, 3903–3945.

14 A. K. Mohammed, J. Raya, A. Pandikassala, M. A. Addicoat, S. Gaber, M. Aslam, L. Ali, S. Kurungot and D. Shetty, *Angew. Chem., Int. Ed.*, 2023, **62**, e202304313.

15 E. J. Jelmy, M. Sunil, C. Kandappanthodi, P. Rincy, K. J. Saji, S. C. Pillai and H. John, *J. Phys. Energy*, 2024, **6**, 025010.

16 Y. Liu, J. Mo, Q. Fu, Y. Lu, N. Zhang, S. Wang and S. Nie, *Adv. Funct. Mater.*, 2020, **30**, 2004714.

17 (*a*) P. Vasandani, Z.-H. Mao, W. Jia and M. Sun, *J. Electrost.*, 2017, **90**, 147–152; (*b*) R. Walden, I. Aazem, A. Babu and S. C. Pillai, *Chem. Eng. J.*, 2023, **451**, 138741; (*c*) A. Chen, C. Zhang, G. Zhu and Z. L. Wang, *Adv. Sci.*, 2020, **7**, 2000186; (*d*) D. T. Mathew, K. V. Vijoy, N. V. Nayar, N. Manoj, K. J. Saji, S. C. Pillai and H. John, *ACS Sustainable Chem. Eng.*, 2022, **10**, 14126–14135; (*e*) S. Joseph, N. T. Padmanabhan, J. Jose and H. John, *Results Eng.*, 2023, **17**, 100869.

18 M. Frisch, G. Trucks, H. Schlegel, G. Scuseria, M. Robb, J. Cheeseman, G. Scalmani, V. Barone, G. Petersson and H. Nakatsuji, *Gaussian 16*, Gaussian, Inc, Wallingford, CT (2016).

19 (*a*) K. Kim and K. D. Jordan, *J. Phys. Chem.*, 1994, **98**, 10089–10094; (*b*) A. McLean and G. Chandler, *J. Chem. Phys.*, 1980, **72**, 5639–5648.

20 A. S. M. I. Uddin, P. S. Kumar, K. Hassan and H. C. Kim, *Sens. Actuators, B*, 2018, **258**, 857–869.

21 G. Min, Y. Xu, P. Cochran, N. Gadegaard, D. M. Mulvihill and R. Dahiya, *Nano Energy*, 2021, **83**, 105829.